論文 / 著書情報
Article / Book Information

Title	Dynamic response analysis of monopile-supported offshore wind turbine on sandy ground under seismic and environmental loads
Authors	Wentao He, Akihiro Takahashi
Citation	Soil Dynamics and Earthquake Engineering, Vol. 189, , 109105
Pub. date	2025, 2
DOI	https://dx.doi.org/10.1016/j.soildyn.2024.109105

Soil Dynamics and Earthquake Engineering 189 (2025) 109105

Contents lists available at ScienceDirect

Soil Dynamics and Earthquake Engineering

journal homepage: www.elsevier.com/locate/soildyn

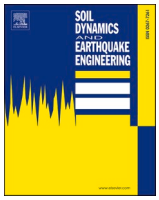

Dynamic response analysis of monopile-supported offshore wind turbine on sandy ground under seismic and environmental loads

Wentao He, Akihiro Takahashi *

Department of Civil and Environmental Engineering, Institute of Science Tokyo, 2-12-1 O-okayama, Tokyo, 152-8550, Japan

ARTICLE INFO

Keywords:
Monopile
Seismic analysis
Offshore wind turbine
Soil-structure interaction
Dense sand

ABSTRACT

Monopiles are the most widely adopted foundation type for Offshore Wind Turbines (OWTs) in shallow waters. With the expansion of the construction of OWT, the number of OWT farms in seismic regions increases globally including the coastal areas of Japan and China. It is necessary to evaluate the impact of earthquakes including the vibration and soil liquefaction on the OWTs supported by the monopile foundation, while the effects of liquefaction on offshore structures, especially for OWTs with monopiles, have not been sufficiently studied. This study investigates the seismic response of the monopile-supported OWTs with the use of an advanced soil model. A three-dimensional numerical model is built, and dynamic analyses are carried out using the OpenSees framework. The pressure-dependent multi-yield (PDMY03) constitutive model is used to simulate the dynamic soil behavior. The applicability of the large-diameter pile modeling method for proper soil-pile interaction modeling in this numerical analysis is first validated through centrifuge tests on monopiles subjected to lateral loading. The dynamic analyses are then carried out to demonstrate the seismic response of the entire OWT system. The numerical results indicate that the contribution of higher modes of vibration is becoming of increased importance for large wind turbines and soil-structure interaction plays a significant role in the dynamic response. Moreover, the monopile-supported OWT in dense sand deposits experiences substantial lateral displacement and rotation under the combined action of wind and earthquake loads when liquefaction occurs.

1. Introduction

Wind power is recognized as one of the most promising alternative and sustainable sources of energy. The utilization of wind energy develops rapidly with its advantages including the vast reserve, minimal environmental impact, and cost-effectiveness [1,2]. From 2000 to 2017, the global wind power capacity approximately doubled every three years, culminating in a total power generation level of 540 GW by the end of 2017 [3,4]. The Global Wind Energy Outlook reports that the total installed capacity of wind power is expected to approach 2000 GW in the world by 2030 and wind energy resources contribute almost 41 % to global installed electricity generation capacity by 2050 under optimistic scenarios [3]. In recent years, wind power farms have begun to move offshore, since wind quality is better in the offshore area, i.e., smoother geography at sea compared to onshore area and stronger and less turbulent wind for large-scale electricity generation [5–8]. Compared with the onshore wind turbines, offshore wind turbines (OWTs) produce 1.7 times more electrical output with 1.2 times faster wind speed [9,10]. Additionally, by relocating the OWTs from 5 km to 10 km further from the coastline, the energy output is expected to increase by 20%–25 %, and the power density is anticipated to rise by 20 % [11]. Offshore wind turbines are thereby increasingly adopted as an important role in future electricity grids due to high energy efficiency and less noise. The offshore wind power industry has experienced rapid development in recent decades, and more than 20 GW of OWTs have been installed all over the world by 2018. It is anticipated that over 520 GW of total installed capacity will be reached by 2050 [12,13].

Most of the existing OWTs are supported by monopile foundations, which are typically hollow steel pipe piles with larger diameters (over 4 m) since they have low construction costs and high bearing capacity [14]. In Europe, 87 % of the market share of the support structure for OWTs is occupied by the monopile foundation by 2017 with a total number of 3720 [15]. Considering the features of offshore wind turbine towers, the effects of environmental load, i.e., wind load and wave load, should be taken into account, thereby the lateral capacity of OWTs is of significant importance. Many researchers have evaluated the lateral capacity of OWTs supported by monopile under the monotonic load and cyclic load conditions through experimental investigations [12,16,17]

* Corresponding author.
E-mail addresses: he.w.fc9c@m.isct.ac.jp (W. He), takahashi.a.3a81@m.isct.ac.jp (A. Takahashi).

https://doi.org/10.1016/j.soildyn.2024.109105
Received 26 September 2024; Received in revised form 6 November 2024; Accepted 19 November 2024
Available online 26 November 2024

and numerical studies [18,19]. Arany et al. [20] summarized a comprehensive and systematic design procedure of the monopile for offshore wind turbines with considering various combinations of environmental load conditions. While this provides a detailed demonstration of the performance of monopiles, it neglects the impact of earthquakes.

In recent years, with the expansion of OWT construction, the number of OWT farms in seismic regions has been increasing globally including the coastal areas of the Yellow Sea and East China Sea of China and the coastal areas of Japan [21]. It seems that the earthquake excitation is deemed to be less relevant for the wind turbine since the low natural frequency, usually identified for the monopile-supported OWTs (e.g., from 0.2Hz up to 0.5Hz) corresponds to the low-intensity part of earthquake motions. However, seismic vulnerability assessment for OWTs gradually received attention with the expansion of the size and number of OWTs, especially for wind farms containing a plethora of large, expensive, and homogeneous OWT structures. Firstly, the seismic response for previous wind turbines of limited height and energy capacity is primarily governed by the first-mode response [22], while this phenomenon is not valid for the modern and higher turbines, in which the higher modes are anticipated to have more significant contribution [23]. The natural frequencies of higher mode are close to the dominant frequency for earthquakes leading to the vibration amplifying due to the resonance. On the other hand, the seismic hazard is recognized as a portion of the integrated multi-hazard environment exposure rather than as an independent disaster for OWTs, meaning that the combined wind-wave-earthquake hazardous environment should be taken into consideration in the assessment of the OWTs' performance.

A series of numerical simulations have been conducted, revealing increased structural demand (i.e., bending moment and shear force) as well as larger response profile (i.e., deflection and rotation angle) for OWTs with monopile caused by the combined effects of environmental loads and earthquakes [24–27]. Liu et al. [24] simulated the OWTs using FAST under the combined earthquakes, wind and wave conditions, and the proposed multiple passive tuned mass dampers (MTMD) can significantly reduce the seismic response of monopile OWTs under those combined loads. Xi et al. [27] developed a framework to conduct an integrated analysis of the NREL 5 MW OWT excited by combined wind-wave-earthquake loading and found that there are significant differences in seismic response between the three operational states (running, parked and emergency shutdown). They concluded that it is hard to determine the most unfavorable condition for the seismic response of the OWT without comprehensive analysis. However, in the models of the two studies above, soil ground is replaced by the coupled spring model and the pile-soil interactions are simulated through the p-y method that cannot capture the characteristic of soil stiffness degradation during the earthquake shaking. Cheng et al. [25] built a coupled numerical model including the wind tower, monopile foundation and soil ground to explore the influence of environmental loads on the seismic response of wind turbines, while the material of soil ground is clay and it adopted the total stress-based model that cannot capture the accumulation and dissipation of pore water pressure.

Undoubtedly, the generation of excess pore water pressure (EPWP) and the potential earthquake-induced liquefaction of the soil ground could adversely affect the lateral capacity or overall stability of the OWT system. Takahashi et al. [16] conducted dynamic centrifuge tests for monopiles in dense sand subjected to two-way lateral cyclic loading, and it stated that the generation of EPWP can lead to the degradation of the soil resistance as well as the lateral capacity of the monopile, although the soil is far from experiencing liquefaction. Carlos et al. [28] performed seismic centrifuge tests for monopiles in layered sand, and great values of excess pore pressure and liquefaction triggered by earthquakes were observed in both loose sand and dense sand. Therefore, an appropriate soil model (e.g., coupled hydro-mechanical (HM) model) developed for the simulation of EPWP and accumulation of shear/volumetric strain in soils susceptible to liquefaction should be adopted in the numerical model. Esfeh and Kaynia [26] investigate the use of advanced liquefaction modeling in the assessment of the response of monopile-supported OWTs, whereas the soil ground in their model is loose sand. Setting up such an easily liquefiable foundation is of little practical significance since monopile is rarely installed under the loose sand condition in actual engineering. Consequently, evaluating the response of OWTs under combined earthquake and environmental load conditions using a coupled HM model in dense sand is desirable, although such analysis has received limited attention so far, and relevant literature is scarce.

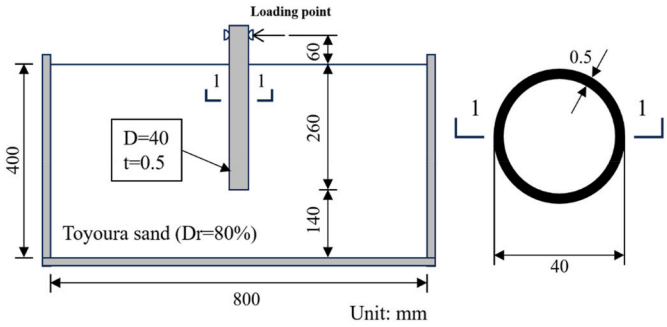

Fig. 1. Schematic diagram of the centrifuge test of monopile in physical model scale.

In this study, the numerical simulation of OWTs using the OpenSees framework [29], involving a fully coupled HM component with an advanced soil constitutive model (PDMY03 soil model) for liquefaction is carried out. The validity and applicability of the large-diameter pile modeling method for proper soil-pile interaction modeling are confirmed by simulations of the centrifuge experiments on monopiles subjected to lateral loading. And then, the established numerical model is utilized in the seismic analysis of a real 3 MW OWT system. The dynamic response of the monopile-supported OWT on sandy ground under seismic shaking is demonstrated. The influences of soil-structure interaction (SSI), environmental load, and soil liquefaction on the seismic response of the entire system are investigated. To gain insight into the performance of OWTs during earthquake shaking, the EPWP, the acceleration, the displacement and rotation angle, as well as the bending moment at several points are computed and compared.

2. Validation of large-diameter pile modeling method

In the numerical model of the monopile-supported OWT, the soil-pile interaction is a critical component. The applicability of the method for considering soil-pile interaction is validated through centrifuge tests on monopiles [30]. Thereby, a three-dimensional finite element analysis is performed to simulate the centrifuge experiments on the lateral behavior of monopile foundations, and then it is validated by comparison with the experimental and simulation results.

2.1. Centrifuge experiments

Results of centrifuge tests conducted by Takeuchi and Takemura

Table 1
Properties of monopiles in the centrifuge test (Prototype scale).

Pile Parameter	Pile-1	Pile-2	Pile-3
Acceleration (G)	25	50	100
Young's Modulus (GPa)	193	193	193
Poisson's ratio	0.3	0.3	0.3
Mass density (kg/m^3)	8000	8000	8000
Diameter (m)	1	2	4
Thickness (mm)	15	30	60
Embedded Depth (m)	6.5	13	26
Loading Height (m)	1.25	2.5	5

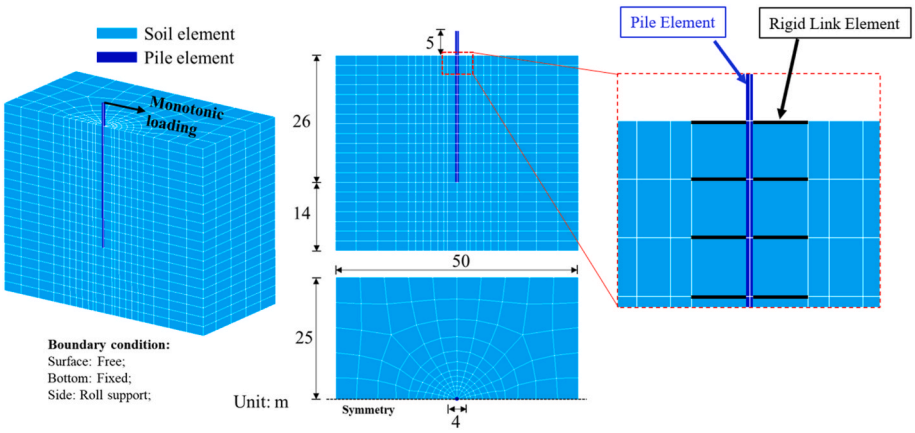

Fig. 2. 3D numerical model for Pile-3 case.

[30] using the Tokyo Tech Mark III centrifuge [31] are utilized to validate the numerical model for the soil-pile interaction. The centrifuge model tests were carried out on three different accelerations (i.e., 25G, 50G, 100G) corresponding to three prototype scales. The tested model in the physical model scale is shown in Fig. 1, while all the test results are shown in the prototype scale for comparison with the simulation results. Each model monopile was placed in the rigid box with inner dimensions of 800 × 250 × 400 mm in the model scale.

The air pluviation method was adopted to prepare the model ground of Toyoura sand with the relative density of D_r = 80 %, and the tests were conducted under dry soil conditions. The monopile used in the test was made of stainless steel with the properties listed in Table 1. One-way cyclic lateral load was exerted with a hydraulic jack in the displacement control. The applied horizontal load and displacement at the loading point were measured by the load cell and laser displacement transducers (LDTs). Since the rate of loading was very slow (0.9 mm/min in the model scale) and the load-displacement curves returned to a unique curve in the reloading processes, the envelope curve of such one-way cyclic load-displacement behavior is treated as the backbone curve and is used for the validation of the numerical simulation. Moreover, the model piles were equipped with strain gauges on both sides of the pile along the loading direction to estimate the bending moment profile. Both measured load-displacement curves and bending moment profiles are compared with the simulation results in the next part.

2.2. Numerical simulations of centrifuge tests

Three three-dimensional numerical models of monopile are built according to the centrifuge tests in the prototype scale. Fig. 2 displays the numerical model of the Pile-3 case with a diameter (D) of 4m. Symmetries of the geometry and loading conditions are exploited for computation efficiency. The length of sides for soil ground is set over 12D, which is large enough to avoid the boundary effect.

The ground is modeled using 8-node, effective-stress solid-fluid fully coupled brick elements, while the fluid pressure in this model is set to be 0 kPa permanently to simulate the dry soil condition. The monopile is simulated using beam-column elements with linear elastic material. The parameters such as Young's modulus, mass density and Poisson's ratio are consistent with those in centrifuge tests tabulated in Table 1. To represent the geometric volume occupied by the monopile, the rigid link elements are installed in the direction normal to the pile's vertical axis connecting the pile elements to the adjacent soil elements [32–34]. Such rigid link elements with extremely high stiffness (10^4 times of the pile element) act together and then each monopile cross-section behaves as a rigid disk, which can reproduce the realistic simulation of the 3D geometry of the soil-pile interface [35]. The connection points on rigid link elements have identical DOF for three translational degrees with the soil nodes, indicating that there is no relative displacement (slippage) between the monopile and soil. As for the boundary conditions, in the fluid part, the fluid pressure of all nodes is set to 0 kPa and remains unchanged to reproduce the dry soil condition. In the mechanical part, the nodes on the bottom side are fixed in three directions, the roll support boundary is applied on the nodes at the side plane meaning that the horizontal movement is restrained while the vertical movement is kept free, and the nodes at the soil surface are kept free, which represent the characteristic of rigid box used in the centrifuge test.

Table 2
Calibrated parameters for Toyoura sand (Dry monotonic condition).

Parameter	ρ_{dry} (ton/m^3)	G_{max_r} (kPa)	B_r (kPa)	φ_{oct} (°)	φ_{PT} (°)	p'_r (kPa)
Toyoura sand	1.56	3.5E4	10.4E4	31	25.5	100

PDMY03 soil constitutive model [36,37] is used to capture the stress-strain behavior of the soil ground. The parameters of the PDMY03 model are calibrated based on the results of laboratory element tests of Toyoura sand with the relative density of D_r = 80 % from the Japanese Geotechnical Society (JGS) standard [38]. Partial parameters are sufficient to describe the soil behavior under the drained monotonic load condition and the calibrated values of the PDMY03 model are shown in Table 2. A comparison of the shear stress-strain and volumetric-shear strain relationships in the octahedral state from the experimental and calculated monotonic drained tests is shown in Fig. 3. The initial stiffness and peak shear strength captured by the PDMY03 model shown in the curves agree well with the measured data, indicating that such calibrated parameters can be used in the numerical simulation.

The simulation results of the monopiles are compared with the measured results in centrifuge tests shown in Fig. 4. For the lateral load-displacement relationships, the non-linear deflection curves are observed for all simulation cases. The numerical simulation reasonably replicates the deformation behavior of Pile-1 and Pile-2, whereas, for the case of the monopile with a large diameter (Pile-3), the simulated results correspond well with the measured results at lower loading levels but gradually deviate at higher loading levels. For the bending moment profiles, several results with different δ (δ is the ratio of lateral displacement at the loading point to the diameter of the monopile) are displayed and the simulated results agree well with the measured results with acceptable deviation. It might be rational to state that the numerical model can capture accurately the soil-pile interaction response of monopile foundations, at least up to an appropriate lateral loading level for large-diameter monopiles. Consequently, such a numerical model is suitable for simulating the real 3 MW monopile-supported OWT described in the following section.

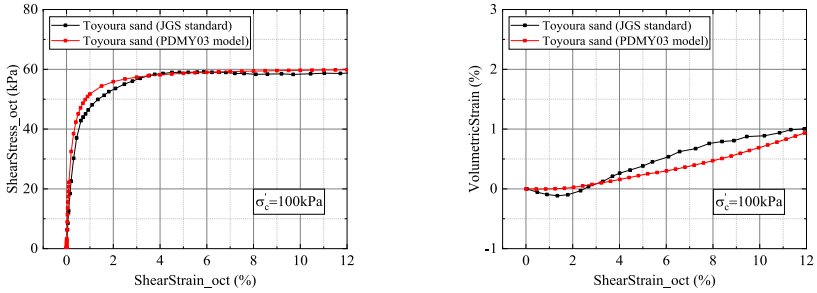

Fig. 3. Comparison between experimental monotonic drained tests and numerical simulations for Toyoura sand.

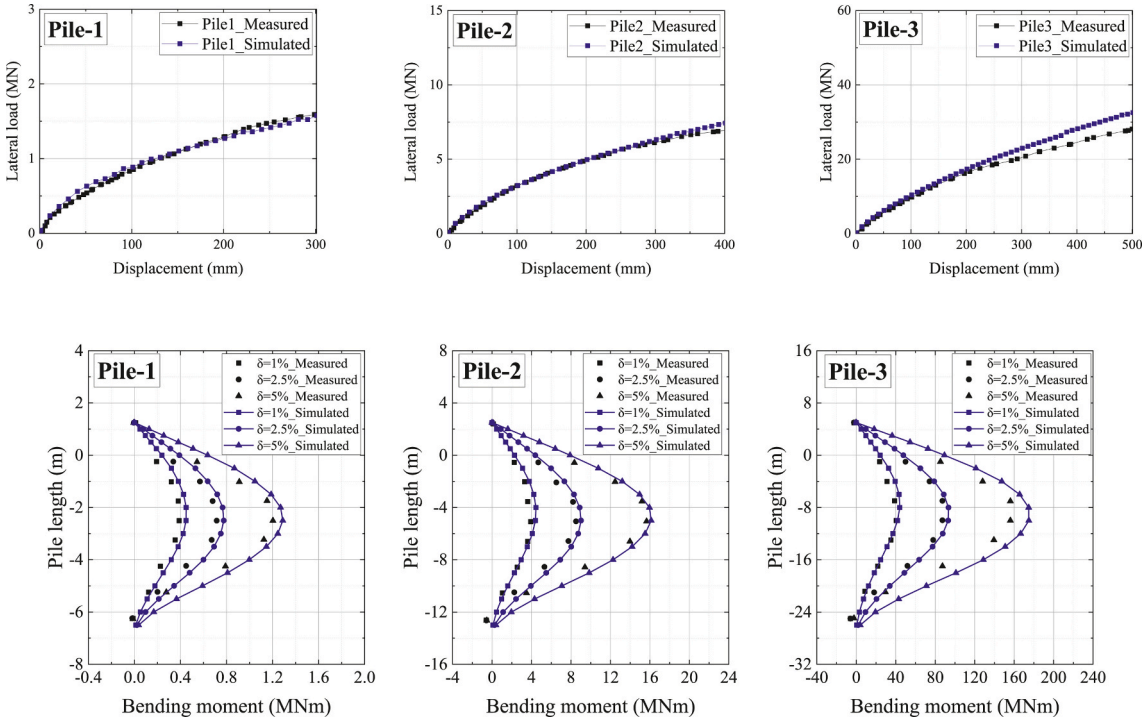

Fig. 4. Lateral load-displacement relationships and bending moment distributions for Pile-1, Pile-2, and Pile-3.

3. Numerical modeling of OWTs with monopile

The dynamic responses of the monopile-supported OWTs subjected to seismic and environmental loads are simulated by employing the numerical model proposed in the former section. A real 3 MW OWT system including the tower, the monopile and the soil ground is built. The setup of the 3D finite element model for dynamic analysis and the load conditions are introduced.

3.1. Finite element modeling

A three-dimensional finite element model of the OWT system is established based on a typical 3 MW offshore wind turbine [20]. The monopile with a diameter (D) of 5.2 m is adopted and the detailed schematic diagram, as well as the geometry of the numerical model, are shown in Fig. 5. The elements used for modeling each component are identical to those in the numerical model described in Section 2.2 (i.e., Beam-column elements for monopile, rigid link and tower; Brick u-p elements for soil ground), while several modifications are applied. Firstly, in the seismic analysis, the saturated soil condition is considered so that the solid-fluid formulation based on Biot's consolidation theory is utilized to simulate the saturated soil domain including displacement and pore water pressure [39]. Next, the boundary conditions for the fluid part are imposed such that the bottom and side boundaries are impermeable while the pore water pressure at the surface node is set to zero and remains unchanged during analysis to replicate the drained condition at the soil surface. Then, certain boundary conditions for the displacement are modified for seismic analysis. The periodic boundary is imposed on the side planes, which ties all the nodes on the side boundary at the same depth to move together in the horizontal direction (i.e., in the X and Y direction) [40] while the vertical movement of those nodes is kept free. Both boundary conditions for fluid and displacement represent the characteristics of the laminar box for the seismic centrifuge test [41,42]. The rotor-nacelle assembly of OWT is modeled as a lumped mass at the tower head of 243 tons. Such simplification for the rotor-nacelle assembly is acceptable since the main purpose of this analysis is to investigate the soil liquefaction, soil-structure interaction (SSI) mechanisms as well as the wind load coupled effect during the earthquake [43–45]. The base shaking is imposed on the bottom nodes of the soil ground with displacement control. OWTs are often recognized as an overall lightly damped system for simplicity and in the numerical simulation Rayleigh damping is assigned to the whole model including

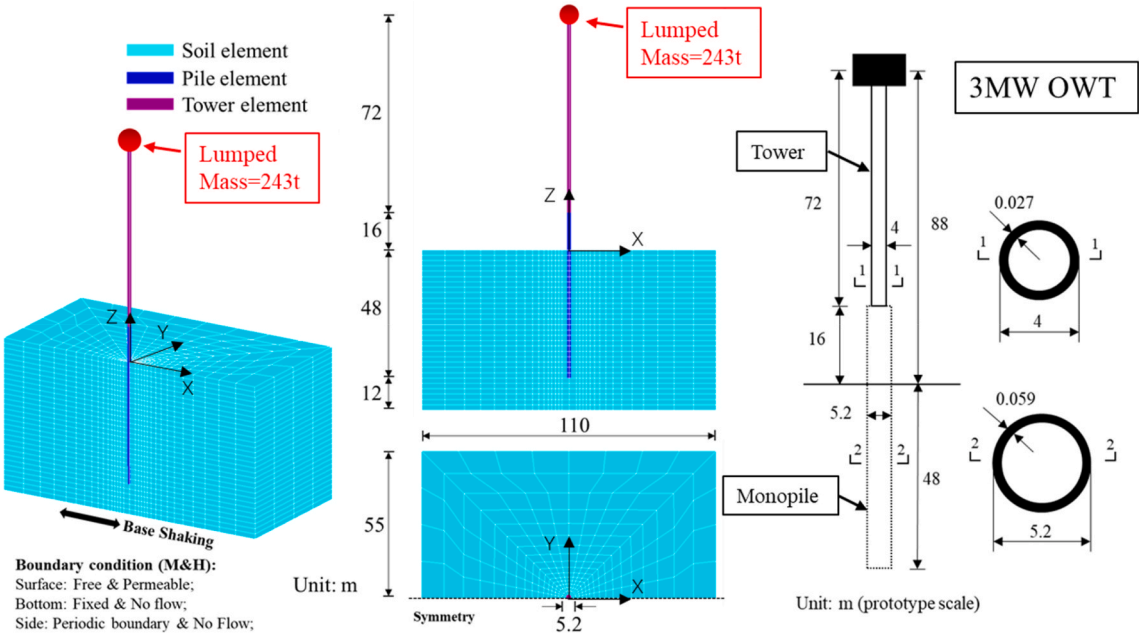

Fig. 5. 3D numerical model & Schematic diagram of 3 MW OWT with monopile.

Table 3
Properties of monopile and tower in the numerical model.

Parameter	Monopile	Tower
Young's Modulus (GPa)	193	193
Poisson's ratio	0.3	0.3
Mass density (kg/m^3)	8000	8000
Diameter (m)	5.2	4
Thickness (mm)	59	27
Mass of the rotor-nacelle assembly (t)	–	243
Bending stiffness (GNm^2)	168.61	132.99

the OWT system and soil ground with a damping ratio of 2 % for the 1st and 6th vibration modes [46,47]. Since the aerodynamic damping of OWTs does not affect the occurrence of soil liquefaction or the impact of unidirectional wind loads on the foundation, it is not considered in this study. The properties of the monopile and tower adopted in the numerical model are listed in Table 3.

PDMY03 soil constitutive model is used to model the soil ground. All parameters are required and used to describe the dynamic behavior of the saturated soil, and then they are calibrated based on the cyclic undrained shear tests [37]. The dynamic behavior of saturated Toyoura sand with a relative density of D_r = 80 % from the laboratory soil element tests conducted by Takahashi [16] and Ueda [48] is considered for the calibration process. Fig. 6 (a) and (b) display the stress-strain relationships and effective stress paths simulated by the calibrated PDMY03 model with CSR (cyclic stress ratio, which is defined as the ratio of the cyclic shear stress generated in the soil to the effective vertical stress) of 0.6 and σ'_{vc} (effective vertical stress) of 50 kPa in cyclic undrained shear loading. The PDMY03 model exhibits the ability to simulate the shear strain accumulation. Fig. 6 (c) shows the generation of EPWP during the cyclic loading. The liquefaction resistance curve for achieving the double-amplitude shear strain of 7.5 % is shown in Fig. 6 (d), and the simulated curve matches the measured data smoothly, indicating that the calibrated PDMY03 model reasonably simulates the dynamic behavior of Toyoura sand under undrained conditions in terms of the liquefaction resistance curve. Additionally, large deformations that occur after sand liquefaction, during which soil progressively accumulates shear strains, can lead to significant damage to structures built in sandy soils [49,50]. Therefore, the accumulated shear strain is an important indicator. Fig. 6 (e) displays the relationship between the number of loading cycles and the accumulated shear strain (single-amplitude shear strain), and relatively good agreement is observed between the simulated and measured results. Moreover, besides the symmetric load condition, the asymmetric load condition is taken into account. Tomasello & Porcino [51] conducted cyclic loading tests of dense silica sand (D_r = 70 %) under an initial static shear stress (a parameter α defined as the ratio of initial static shear stress acting on a horizontal plane to the initial effective overburden stress). The accumulated shear strain under both symmetric (α = 0) and asymmetric (α = 0.2) load conditions is shown in Fig. 6 (f). Although discrepancies between the simulated and measured results exist due to differences in relative density between the experiment and simulation, a similar trend is observed that the existence of initial static shear negatively affects the cyclic resistance for small and moderate strain levels while being beneficial at large strain levels for dense sand [52]. Finally, the calibrated parameters of the PDMY03 model for Toyoura sand with a relative density of 80 % are shown in Table 4. It should be noted that the calibrated parameters are based on cyclic laboratory test data, which accounts for some differences observed in the parameters calibrated from monotonic tests listed in Table 2.

3.2. Loads and analysis cases on the OWT system

Before conducting seismic analysis, the acceleration time history of white noise excitation is used to identify the dynamic characteristics of the systems as shown in Fig. 7 [42,53]. The frequency range of the white noise excitation spans from 0.1 Hz to 30 Hz, which is used to obtain the natural frequency of the entire model. Additionally, the amplitude of the white noise excitation is kept very low (0.025 g) to ensure that the model is in the small strain level of elastic state without any damage or plastic deformation and no excess pore water pressure generated in the soil ground.

Then, the Tokachi-Oki earthquake (NS component) recorded at Hachinohe Port in 1968 is used as the seismic excitation. The specific seismic record is widely used in the seismic design of high-rise buildings and high-standard levees in Japan so it is suitable for the OWT with applying this earthquake shaking record. The acceleration time history and Fourier spectra of the Tokachi-Oki earthquake are shown in Fig. 8. The peak ground acceleration (PGA) is 0.239 g. The continuous range

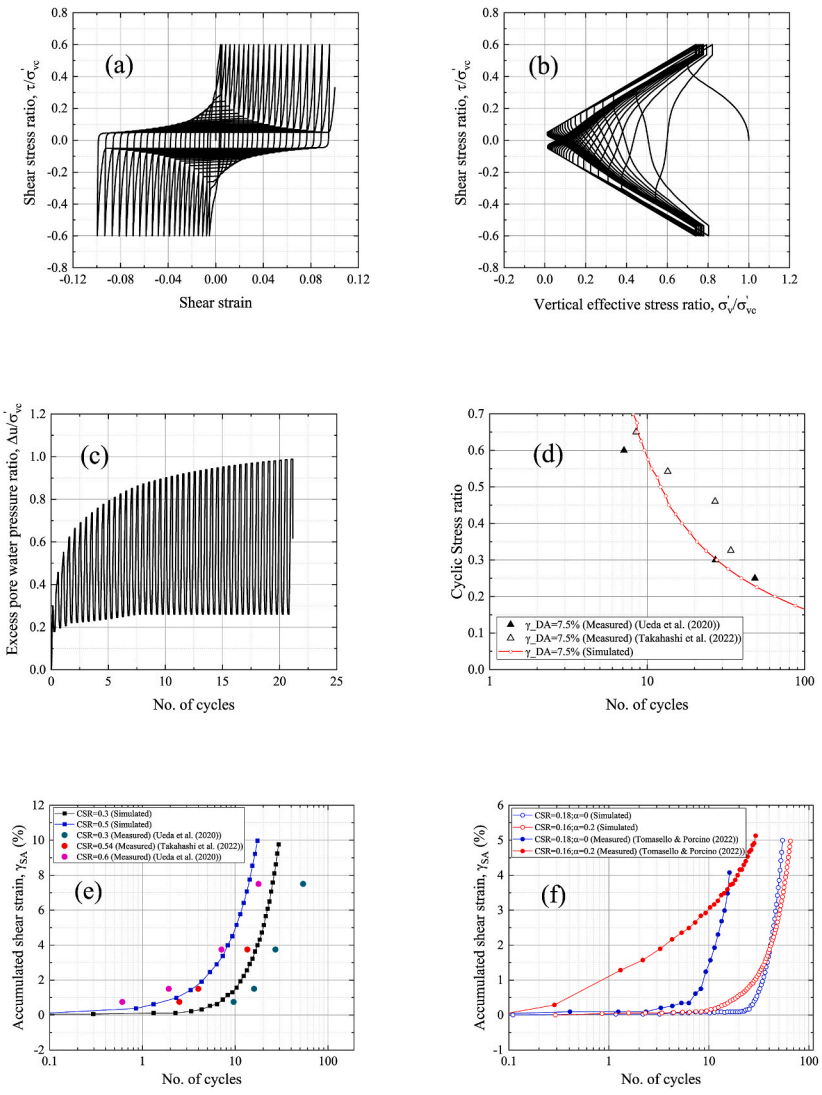

Fig. 6. The dynamic response of the calibrated PDMY03 model at the element level.

Table 4
Calibrated parameters for Toyoura sand (Saturated cyclic condition).

Parameter	ρ_{sat} (ton/m^3)	G_{max_r} (kPa)	B_r (kPa)	φ_{oct} (°)	φ_{PT} (°)	p'_r (kPa)	k (m/s)	c_a	c_b	c_c	c_d	c_e	d_a	d_b	d_c
Toyoura sand	1.97	9.0E4	28.4E4	32.5	25.5	100	2.0E-4	0.007	2.0	0.5	6.0	−0.05	0.45	1.0	−0.3

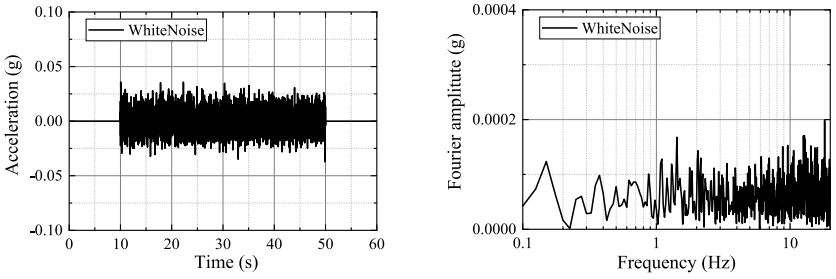

Fig. 7. Acceleration time history and Fourier spectra of input white noise.

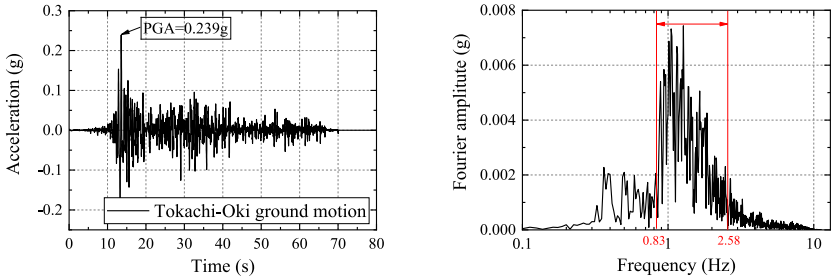

Fig. 8. Acceleration time history and Fourier spectra of the Tokachi-Oki earthquake.

Table 5
Analysis cases on the OWT system.

No.	Ground condition	Load condition
Case 1	Saturated soil	Wind load
Case 2	Saturated soil	Wind & Earthquake load
Case 3	Saturated soil	Earthquake load
Case 4	Fixed base	Earthquake load
Case 5	Fully drained	Wind & Earthquake load
Case 6	Fully drained	Earthquake load

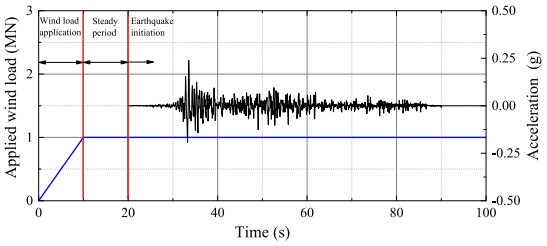

Fig. 9. Load pattern for the earthquake and wind loads.

where the Fourier amplitude exceeds 0.002 (approximately a quarter of the maximum amplitude) in the frequency spectrum diagram is regarded as the dominant frequency, spanning from 0.83 Hz to 2.58 Hz.

In reality, an earthquake event occurs during the lifetime of the OWTs, and thereby certain environmental loads (e.g., wind load & wave load) are also exerted on the structure simultaneously. It is noted that the probability of occurrence of earthquakes and extreme ocean conditions simultaneously is extremely low, thereby consideration of normal ocean conditions is sufficient. Under these circumstances, the contribution of wind loads to the internal forces (bending moment) at the mudline cross-section of the monopile is significantly greater than that of wave loads. Meanwhile, compared to wave loads, which have a maximum period of about 10 s, wind loads have a longer period exceeding 100 s [20]. Therefore, the wind load is simulated as a constant load in a simplified manner, without taking the wave load into account in the numerical simulation at this stage. The application of time-variant wind and wave loads coupled with the seismic load in the transient analysis will be one of the future assignments. The wind load is calculated by the rated wind speed for 3 MW OWT of 12 m/s based on the IEC code and applied at the tower head [54]. A design wind load of 1 MN is assumed [20,35]. Meanwhile, to evaluate the effect of soil-structure interaction and soil liquefaction on the dynamic response of the OWT, fixed base and full drain soil conditions are also considered. Consequently, totally six different loading scenarios with various ground conditions are conducted and tabulated in Table 5. In Case 2, the

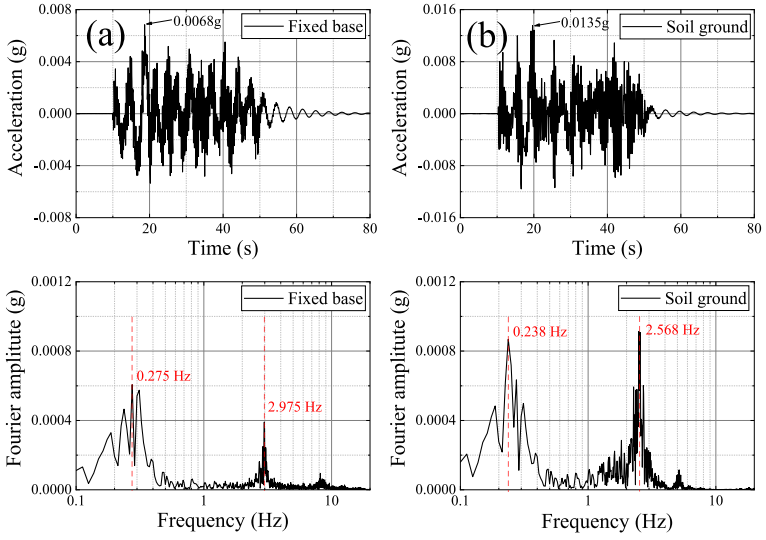

Fig. 10. Acceleration time history and Fourier spectra at tower head during white noise excitation: (a) fixed base; (b) soil ground.

purpose is to emphasize the combination effect of the seismic and wind loads on OWT. In Case 3, seismic shaking is applied in the absence of wind loads allowing assessment of the pure seismic response of the OWT. In Case 4, a fixed base condition is adopted. The entire structure below the mudline is removed and a rigid base is used for the remaining portion, meaning that the soil-structure interaction is neglected. In Cases 5 and 6, soil liquefaction does not occur since a very large hydraulic conductivity is applied, and the simulation results from these cases are utilized for comparison and evaluation of the influence of soil liquefaction. It is noted that the initial effective stress distribution in the fully drained conditions is identical to Cases 1–3. For the load condition including both wind and earthquake loads, the load pattern is performed in three steps as shown in Fig. 9. In the first step, the wind load is gradually applied from zero up to the preset value and then this load is kept the constant, followed by a steady period to eliminate any external acceleration and bring the model into a stable state in the second step. Finally, the earthquake shaking record as shown in Fig. 8 is applied in the third step under the existence of wind load acting at the identical direction, while it is a very conservative operating condition. The total simulation time is 100 s with a time step of 0.008 s.

4. Results and discussions

The dynamic characteristics of the OWT system including natural vibration modes is analyzed. Then, the seismic responses of the soil ground such as the generation of the EPWP and the time-history of the shear stress-strain relationship are discussed. Finally, the seismic performance including the acceleration, lateral displacement, rotation angle, and bending moment of the monopile-supported OWT is compared to discuss the influence of soil-structure interaction (SSI), wind load, and soil liquefaction.

4.1. Eigenvalue analysis and natural frequency

Eigenvalue analysis is performed to receive the natural frequency describing the dynamic characteristics of the entire system. White noise mentioned in Section 3.2 is adopted as input base shaking. The acceleration time history at the tower head is recorded, and then the Fourier transform spectrum is calculated based on the recorded time history data as shown in Fig. 10 to obtain the natural frequencies from several peak values in the spectrum. Both fixed base and soil ground conditions are simulated to highlight the effect of the SSI on OWTs. Based on the Fourier transform spectra, it appears that with the fixed base condition, the first and second-order natural frequencies are 0.275 Hz and 2.975 Hz, while with the soil ground condition, i.e., taking the SSI into account, these values are 0.238 Hz and 2.568 Hz. The natural frequencies of OWT considering soil ground are smaller and reduced by 13.4 % for the first mode and 13.7 % for the second mode, respectively. The numerical model with a fixed base condition overestimates the natural frequency of monopile-supported OWTs, as it assumes the soil constraint effect to be infinite [55]. Compared to the fixed base, soil ground is softer to decrease the stiffness of the whole model leading to the reduction of natural frequency [56]. Álamo et al. claimed that the effect of the SSI can decrease the fixed-base natural frequency of the offshore wind turbine by more than 15 % in the frequency range above 0.25 Hz [57]. Moreover, in the event of soil liquefaction during a strong earthquake, the natural frequency of the entire system will drop even further since the soil ground adjacent to the foundation of OWTs loses its strength along the liquefaction zone leading to unanticipated fatigue damage [58]. In addition, the response amplification driven by the SSI is observed by comparing the peak acceleration and Fourier amplitude between models of the fixed base and soil ground conditions. A larger dynamic response at the tower head is obtained using a soil ground model due to the kinematic SSI and a fixed base model will underestimate the seismic response, which is harmful to the structure design [56, 59]. Consequently, in the seismic and frequency analysis for the OWT, it

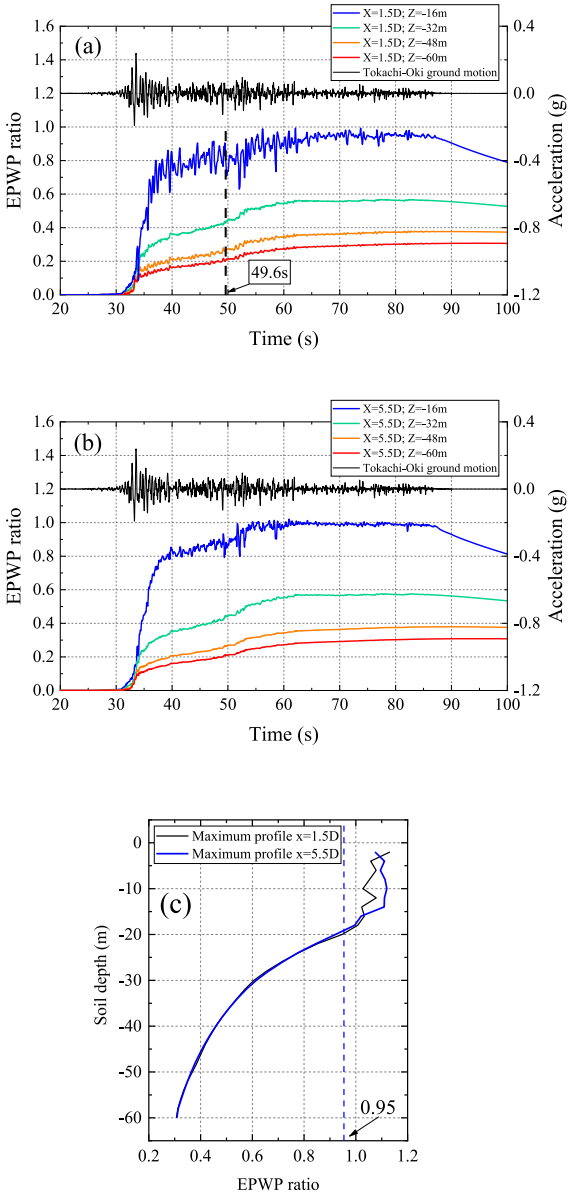

Fig. 11. (a) Time histories of EPWP ratio at different depths in the near field; (b) Time histories of EPWP ratio at different depths in the far field (c) Maximum EPWP ratio profiles.

is necessary to take the SSI into account integrally including a rational and accurate description of the soil properties.

On the other hand, it appears that the first mode dominates the dynamic performance under the fixed base condition, while the first and second modes take almost equal share of the whole dynamic performance with the soil ground condition. This suggests that for the huge and modern offshore wind towers, higher modes are anticipated to make a more significant contribution to the dynamic response. Sah and Yang conducted a series of numerical simulations with various foundation types and concluded that simplified foundation models such as fixed base ground are not accurate enough and ignoring higher modes may lead to the underestimation of the base shear and overturning moment [60]. Higher mode effects also can amplify the seismic response when the natural frequencies of higher modes tend to closely align with the dominant frequency range of the earthquake, potentially leading to resonance [61]. For instance, the second-order natural frequency with

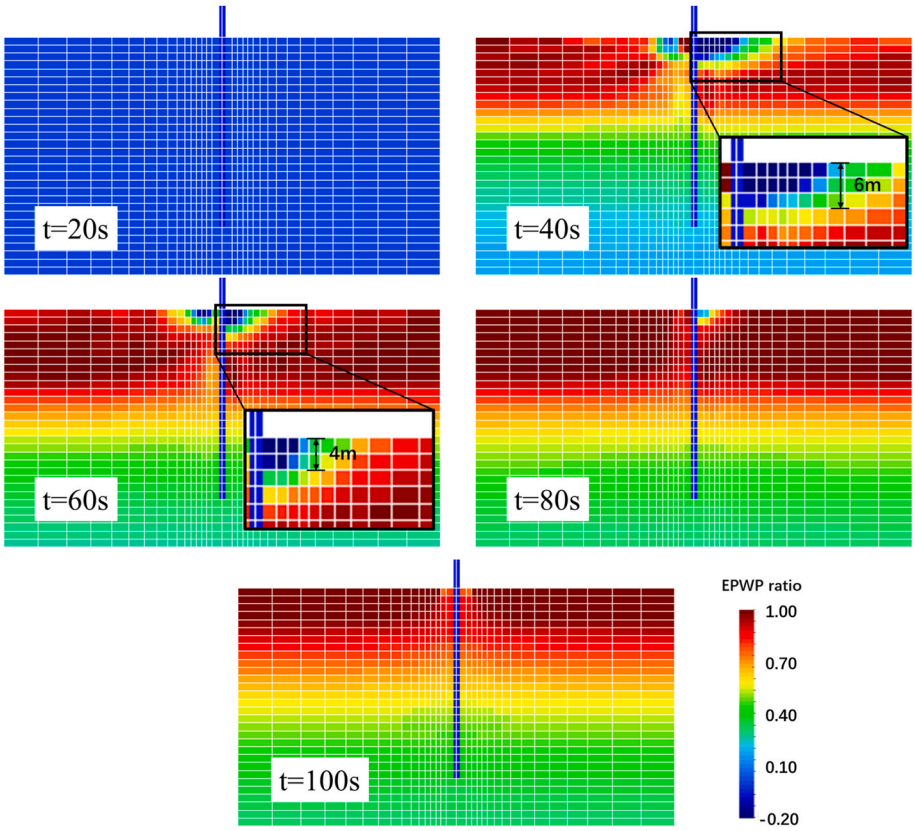

Fig. 12. Distribution of EPWP ratio in the x-z plane of the soil-pile model under Tokachi-Oki ground motion at times 20, 40, 60, 80, and 100 s.

the soil ground condition is 2.568 Hz, which is located in the dominant frequency range of the Tokachi-Oki earthquake as shown in Fig. 8 and it is assumed that resonance appears during the earthquake shaking.

4.2. Excess pore water pressure

During the dynamic event, excess pore water pressure (EPWP) plays an essential role in the evaluation of soil liquefaction. The excess pore pressure in this section is presented in terms of excess pore pressure ratio (EPWP ratio) defined as $r_u = \Delta u/\sigma'_{v0}$ (where σ'_{v0} is the initial effective vertical stress at a certain depth, Δu is the EPWP). The limit $r_u = 0.95$ is regarded as a liquefaction criterion i.e., the soil liquefaction occurs when r_u exceeds 0.95. The monotonic wind load does not cause any liquefaction on the soil ground, so the effect of the earthquake only is taken into account in this section (Case 3) and the Tokachi-Oki ground motion mentioned in Section 3.2 is adopted as the input base shaking. Fig. 11(a) and (b) display the time histories of EPWP ratio with various depths at the near field, i.e., the location near the foundation that is 5.2 m away from the edge of the monopile (X = 1.5*D*) and at the far field (X = 5.5*D*), respectively. It appears that with the initiation of the earthquake at 20 s and gradual enhancement of shaking after 30 s, the corresponding EPWP ratio dramatically increases at both near field and far field and the soil reaches the liquefaction state after 50 s at the soil depth of 16 m. Although dense sand, such as Toyoura sand with a relative density of 80 %, is not typically regarded as liquefiable sand, the occurrence of liquefaction in such dense sand is acceptable and rational. Ueda et al. [48] performed seismic centrifuge tests on offshore wind turbine systems in Toyoura sand of *Dr* = 80 %, and soil liquefaction was observed in the dense sand during moderate earthquake shaking. In the deep soil layers (i.e., depth of 32, 48, 60 m), there exists no considerable difference between the time histories of EPWP ratio, while in the shallow soil layers (i.e., depth of 16 m), more fluctuations and oscillations are observed in the near field, and they are attributed to the SSI, including the vibration of the monopile and superstructure. In addition, Fig. 11(c) shows the maximum EPWP ratio profiles along the soil depth at near and far fields to have detailed observations about the soil liquefaction. The shallower the soil ground, the higher the EPWP ratio, as at deeper levels, the substantial gravitational stress limits the development of this ratio, thereby preventing soil liquefaction. Conversely, soil liquefaction occurs in the shallow part (above 20m of soil ground) leading to the degradation of soil stiffness, which is harmful to the OWT subjected to the lateral wind load.

Fig. 12 illustrates the distributions of the EPWP ratio, which allows an understanding of the development and dissipation of the EPWP over time. Besides the development of EPWP due to seismic shaking, negative pore water pressure appears around the monopile in the surface soil layers (i.e., depth of 6 m). The negative pore water pressure is generated by the vibrated monopile. When the soil is compressed laterally by the monopile on one side, negative pore water pressure is generated on the opposite side due to the dilation and unloading of the soil in that area. This phenomenon was observed by many researchers in the experiment [16,28] and numerical simulation [62,63]. The soil dilation in the dense sand can lead to a stiffer dynamic response for the entire system since the negative pore water pressure makes the soil ground adjacent to the monopile stiffer by increasing the effective stress. Meanwhile, it should be mentioned that no relative displacement (slippage) at the monopile-soil interface is allowed in the numerical model, which means that the gap between the monopile and adjacent soil cannot be simulated. The soil elements on the unloading side are dragged by the vibrated monopile, which can enhance the dilation and lead to an overestimation of negative pore water pressure.

4.3. Shear stress-strain response of soil near the monopile

The shear stress-strain responses with (Case 2) and without (Case 3) considering wind load in the saturated soil ground during the Tokachi-

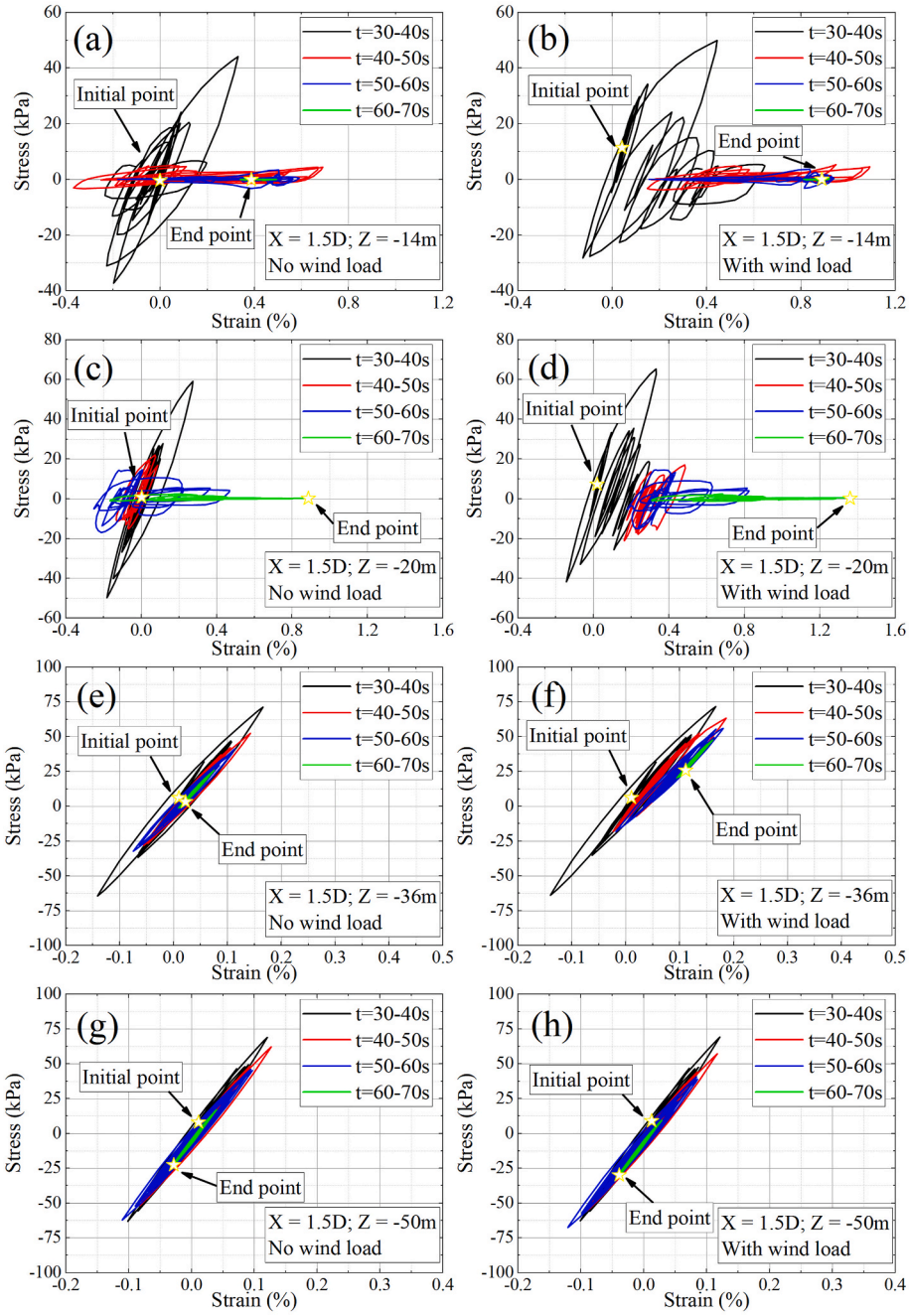

Fig. 13. Shear stress-strain responses at different depths for various periods with and without considering wind load.

Oki ground motion are recorded with different depths at the near field (X = 1.5*D*) on the leeward side (i.e., the soil around this side is compressed laterally by the monopile). The influences of soil liquefaction and lateral wind load are investigated for various periods as shown in Fig. 13.

Distinct colors are utilized to delineate time intervals of 30–40 s, 40–50 s, 50–60 s, and 60–70 s, which are associated with the initial generation (30–40 s), subsequent development (40–60 s), and ultimate peak (60–70 s) of EPWP. The initial points as well as the endpoints of the time range from 30s to 70s are highlighted in graphs. In the soil layer (Z = −14m & −20m shown in Fig. 13(a)–(d)) where the soil liquefaction occurs, the curves clearly illustrate the change in the response pattern and the reduction of the soil stiffness due to generation of EPWP and seismic shaking. The shear stress-strain relationships transition from the conventional symmetrical behavior (black curves) to a more yielding behavior (red and blue curves), characterized by a decrease in shear stress and an increase in shear strain. Finally, the response pattern evolves into a flat loop located on the horizontal axis where the shear stress is equal to zero reflecting the full soil liquefaction state with negligible soil stiffness (green curves). In the soil layer (Z = −36m & −50m shown in Fig. 13(e)–(h)) without the occurrence of soil liquefaction, the tendency of the shear stress-strain response pattern across all time windows seems to be consistent, maintaining specific soil stiffness throughout. This suggests that the soil at these depths retains its stiffness during the earthquake shaking.

Moreover, the effect of the wind load on the shear stress-strain behavior is distinct, especially in the soil layer with liquefaction (Z = −14m & −20m). A significant increase in shear strain is observed in the case with wind load during the time windows of 40–50 s, 50–60 s, and 60–70 s when the EPWP progressively increases and reaches the

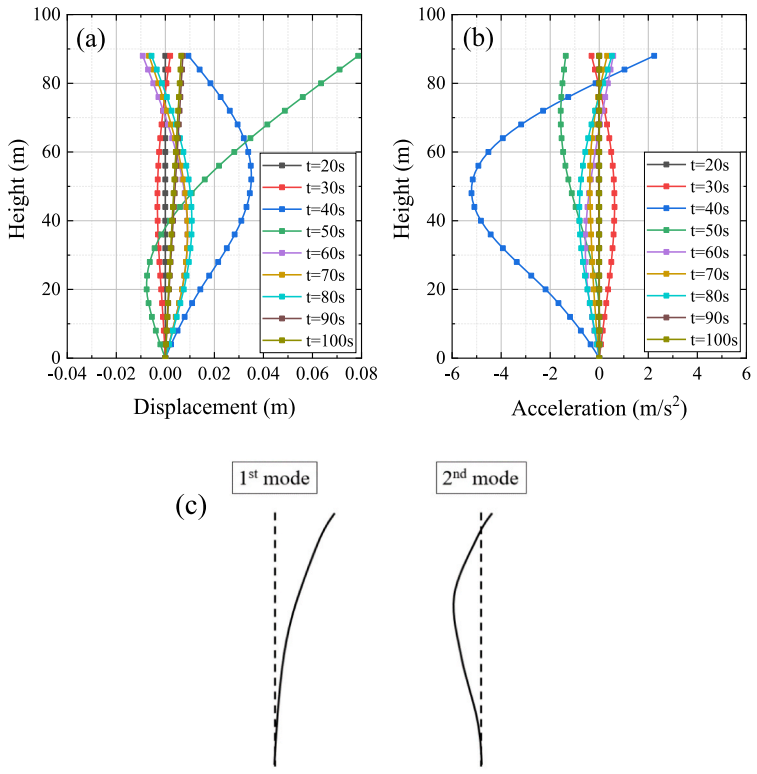

Fig. 14. Profiles of (a) horizontal displacement, (b) horizontal acceleration of the OWT at various time steps and (c) schematic diagram of shapes for first and second modal.

maximum value. Considering wind loads, the soil elements on the leeward side are compressed by the monopile laterally, and combined with such deviatoric stress caused by the compression, the shear strain of soil increases further during liquefaction, as the soil stiffness becomes negligible. In contrast, the difference in soil behavior caused by wind loads is not obvious in the deep soil layer without liquefaction (Z = −36m & −50m) since the soil still retains its stiffness. Consequently, based on the behavior of the soil element adjacent to the monopile, it is inferred that the entire OWT system will undergo a relatively considerable lateral displacement under the combined effects of wind and seismic loads.

4.4. Seismic performance of OWT and monopile

Firstly, the impact of solely the earthquake on the dynamic response of the OWT is demonstrated (Case 3). The relative horizontal displacement and acceleration profiles to the mudline location (Z = 0) of the OWT at various time steps as well as the first two modal shapes are shown in Fig. 14. By comparing the shapes of the two modes (Fig. 14(c)), it is observed that the second vibration mode is dominated in the dynamic response during the shaking (Fig. 14(a)) and maximum acceleration appears at the middle location of the OWT rather than the tower head (Fig. 14(b)) since the second-order natural frequency of the entire system is located in the dominant frequency range of Tokachi-Oki ground motion as mentioned in Section 4.1. Therefore, it is insufficient to merely focus on the displacement and acceleration at the tower head (Z = 88m) although important equipment such as rotor-nacelle assembly is installed there. The dynamic response at the middle (Z = 44m) and transition piece (Z = 16m) connecting the monopile and the tower should also be taken into consideration.

Fig. 15 displays the displacement and acceleration time histories, along with the Fourier spectra of the acceleration during Tokachi-Oki ground motions at various heights (Z = 0m, 16m, 44m, 88m) of the OWT and the results at the mudline height (0m) is also plotted as a reference for comparison. The time histories of displacement and acceleration recorded at the heights of 88 m and 0 m are generally similar in shape. However, in the frequency domain, the value at 88 m shows attenuation around the peak frequency and amplification near the second vibration mode (2.568 Hz) is observed when compared to those at 0 m. At the height of 16m and 44m, amplifications are observed in both the time and frequency domains with the factor of 2 and 4 in the acceleration time histories, respectively. Especially, a significant amplification appears near the second vibration mode (2.568 Hz) at the height of 44m, and it seems that resonance happens during the seismic shaking. Meanwhile, the amplification impact on the displacement and acceleration at the transition piece (Z = 16m) should not be neglected since the entrance door allowing access to the rotor-nacelle assembly part of the OWT is placed there with an opening, which constitutes the structural weakness including the stress concentration [64] and low buckling capacity [65].

Then, the impact of the soil-structure interaction (SSI) during the seismic shaking on the OWT is evaluated based on the simulated results of Cases 3, 4 and 6. Time histories of displacements and accelerations at the tower head of the OWT are shown in Fig. 16. It is observed that the amplitudes of the simulated displacement and acceleration under the fixed base ground (Case 4) are extremely small compared to the saturated soil ground case (Case 3), which emphasis the amplification impact of the SSI. Medina et al. [66] conducted a series of numerical simulations to study the effect of SSI on the seismic response of large monopile-supported OWT and concluded that SSI, especially the rotational kinematic interaction, can amplify the OWTs' seismic response. In Case 4, there is no kinematic interaction between the soil and underground foundation, resulting in the minimum dynamic response, while in Cases 3 and 6, they include the soil ground part meaning that there

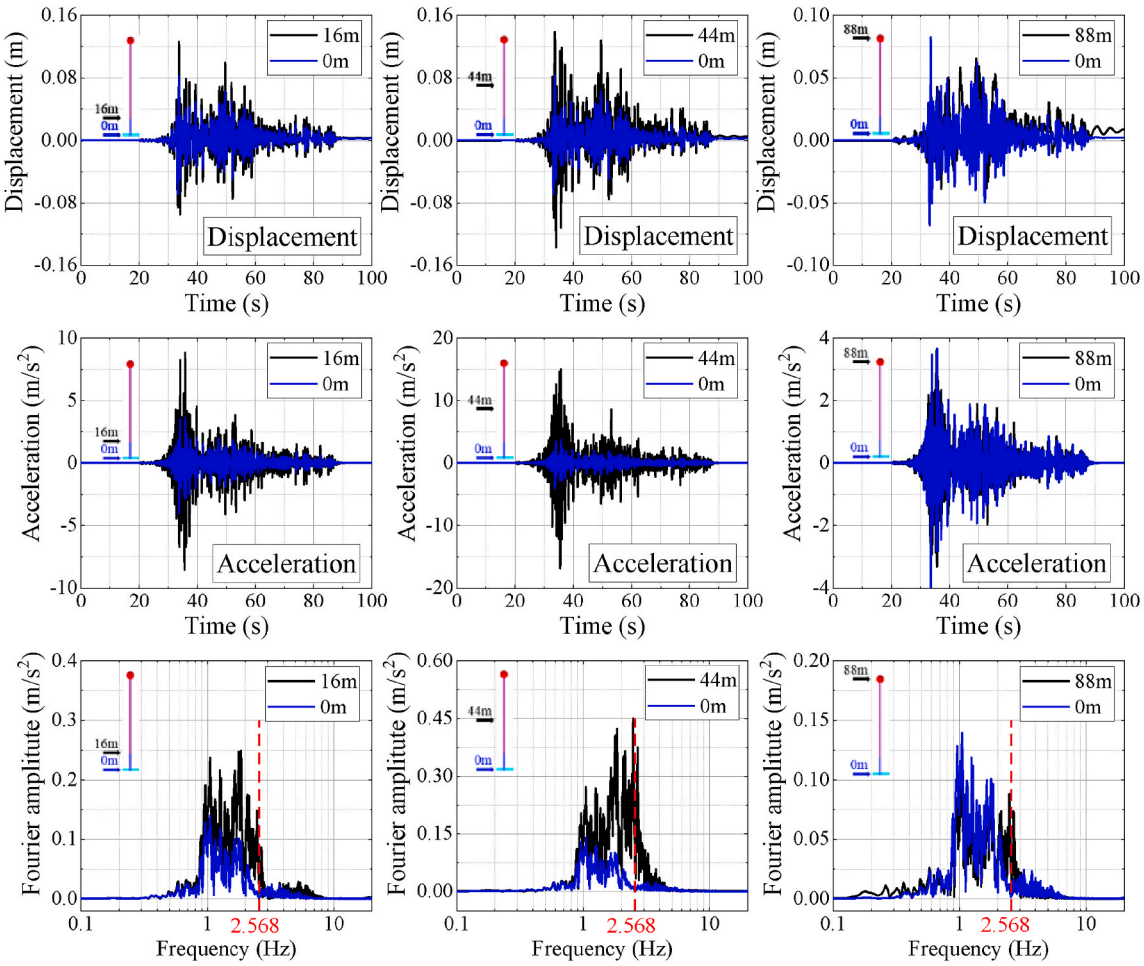

Fig. 15. Displacement and acceleration time histories as well as Fourier spectra during Tokachi-Oki ground motions at various heights of the OWT.

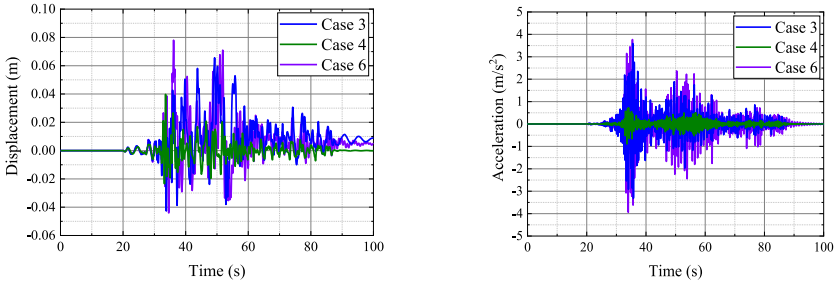

Fig. 16. Displacement and acceleration time histories during Tokachi-Oki ground motions at the tower head of the OWT.

exists kinematic interaction. As for the full drain soil ground condition (Case 6) in which change in pore water pressure is not considered, the simulated results show that both displacement and acceleration are slightly larger than the results of the saturated soil ground condition (Case 3) due to no decaying effects on kinematic interaction caused by the EPWP generation [67]. Bending moment and shear force time histories at the mudline of the OWT are shown in Fig. 17. Since these forces are affected by the inertial force of the superstructure, a similar tendency in amplitude is observed as seen in the acceleration time histories. These suggest that neglecting SSI leads to an underestimation of the dynamic response of the monopile-supported OWT as also mentioned in Section 4.1.

Finally, the impact of the wind load during the seismic shaking on the OWT is evaluated based on the simulated results of Cases 1, 2, 3 and 5. Serviceability limit states (SLS), which represent criteria governing normal functional or operational use, are considered in this case based on Design codes such as DNV-OS-J101 [68] and DNV-RP-0585 [69] to evaluate the seismic performance of the monopile-supported OWT: (1) Lateral deflection at the mudline must be less than 0.2 m, (2) Rotational tilt must at the mudline be less than 0.5°. Fig. 18 displays time histories of lateral displacements and rotations of monopile at the mudline (Z = 0m) for Cases 1, 2 and 3, respectively. Since the application of the wind load remains constant after 10 s, the lateral displacement and rotation in Case 1 are straight lines from 20 to 100 s. As for the results in Case 2, it appears that the tendencies of both lateral displacement and rotation gradually deviate and increase after 30 s at which the EPWP begins to

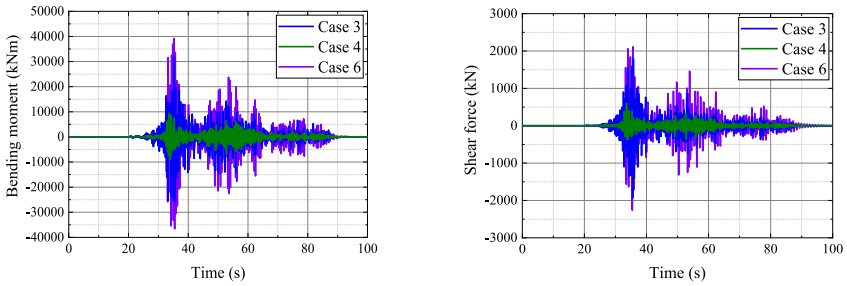

Fig. 17. Bending moment and shear force time histories during Tokachi-Oki ground motions at the mudline of the OWT.

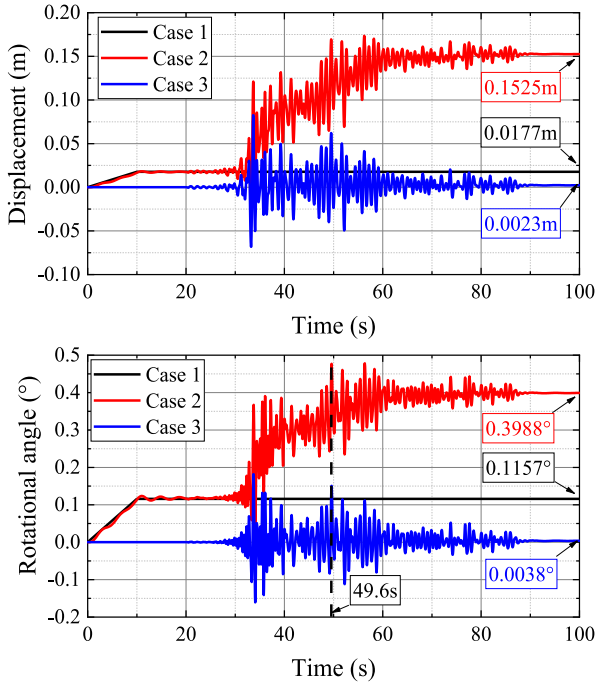

Fig. 18. Displacement and rotational angle time histories in Cases 1, 2 and 3 at the mudline of the OWT.

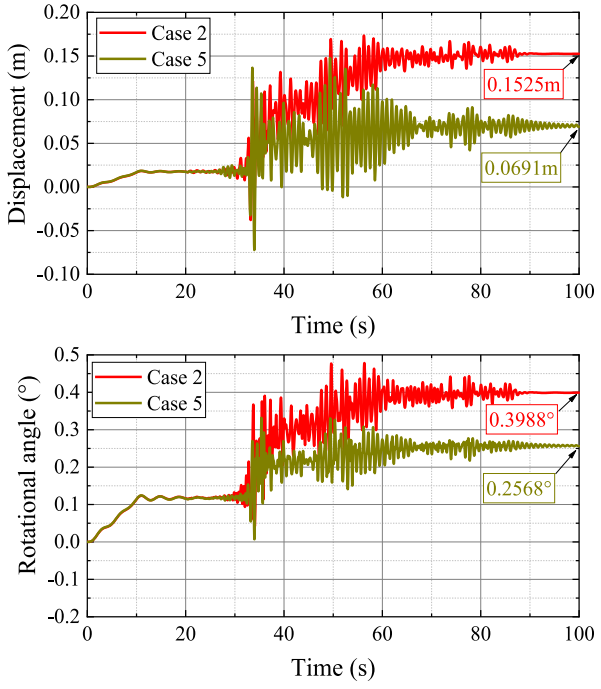

Fig. 19. Displacement and rotational angle time histories in Cases 2 and 5 at the mudline of the OWT.

increase (Fig. 11(a)). With the generation of EPWP, the soil stiffness is decreased leading to the reduction of the lateral capacity of the monopile. Consequently, the larger lateral displacement and rotation occur under the combination of the earthquake and wind loads in Case 2, compared with the results in Case 3 with the application of earthquake alone. Fig. 19 displays time histories of lateral displacements and rotations of monopile at the mudline for Cases 2 and 5. Deviations in lateral displacements and rotations are observed in these two cases with larger deviations in Case 2 due to soil liquefaction. This shows that soil liquefaction also makes a significant contribution to the development of lateral displacements and rotations of the monopile.

The maximum displacements and rotations as well as residual displacements and rotations for all three cases are tabulated in Table 6 for quantitative comparisons. The values in Case 2 are significantly larger than the arithmetic sum of the values from Case 1 and Case 3 shown in the parentheses meaning that the impact of the coupled wind and earthquake loads on the monopile-supported OWT is not the linear superposition. The calculated displacements and rotations of all three cases can satisfy the requirement of SLS in this numerical model, but those results are not so accurate compared to the OWT under the real offshore environment since the wave load is neglected in the simulation. Moreover, it should be emphasized that the combined effect of wind and earthquake loads can lead to severe deflection because of the soil

Table 6
Displacement and rotation of the OWT at the mudline.

Case	Displacement (m)		Rotation (°)	
	Maximum	Residual	Maximum	Residual
Case 1	0.0177	0.0177	0.1157	0.1157
Case 2	0.1730	0.1108	0.4725	0.3988
	(0.1001)	(0.0200)	(0.2976)	(0.1195)
Case 3	0.0824	0.0023	0.1819	0.0038
Case 5	0.1476	0.0691	0.3264	0.2568

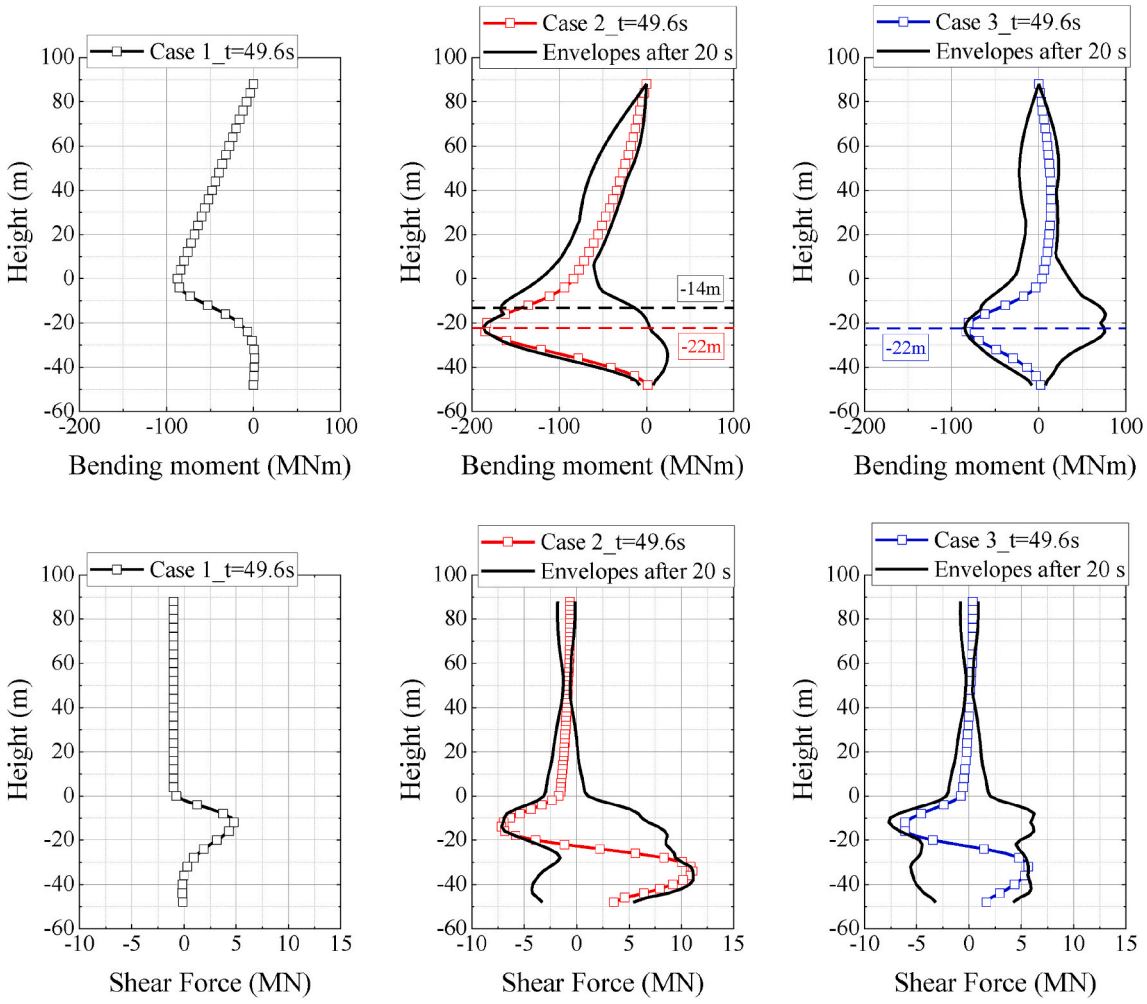

Fig. 20. Bending moment and shear force profiles at 49.6s together with the maximum and minimum envelopes.

liquefaction during the earthquake, which cannot be ignored in the design for monopile-supported OWTs constructed in highly seismic regions.

In Fig. 20, the bending moment and shear force profiles of all three cases at the time of 49.6 s, corresponding to the time when the peak rotational angle is observed in Case 2 as shown in Fig. 18, are plotted. Envelopes of the maximum and minimum bending moment and shear force during shaking (after 20 s) are also shown for Cases 2 and 3.

In Case 1, the bending moment at the pile tip is zero, i.e., the moment resistance at the pile tip is insignificant. This is because the slenderness ratio (L/D, where L = embedment length of the pile and D = pile diameter) of the monopile in all the cases is 48/5.2 = 9.23 and the monopile in this study is categorized as the slender pile [16,20]. However, a large shear force is observed at the pile tip for Cases 2 and 3 with the earthquake loads, and it is attributed to the kinematic interaction between the pile and soil during the seismic shaking.

Due to the wind load, the largest negative (the absolute maximum) bending moment appears around the mudline as seen in the case with the wind load only (Case 1). As mentioned above, it is not a simple superposition but the response in Case 2 can be viewed as a combination of those in Cases 1 and 3. Because of this, the absolute value of the minimum bending moment for Case 2 is larger than that in Case 3, while that of the maximum bending moment is smaller, as observed in the bending moment envelopes line.

Meanwhile, almost all of the shear force is positive below the mudline in Case 1 because of the wind load. Due to the combination effect of earthquake and wind loads, the value of the maximum shear force for Case 2 is larger than that in Case 3, while the absolute value in the minimum shear force is slightly smaller as observed in the shear force envelopes line.

At 49.6 s, soil liquefaction occurs, as shown in Fig. 11 (a). Such liquefaction in the shallower depth reduces the soil stiffness, resulting in the largest absolute value in the minimum bending moment appearing at a depth comparable to the bottom of the liquefied zone (Z = −22 m) as shown in Fig. 11 (c).

Comparisons between Cases 2 and 3 reveal that the maximum absolute values of bending moment and shear force in Case 2 are always larger than in the other two cases due to the coupled wind and earthquake loads. Consequently, the simulation of these three cases highlights that the combined effect of the earthquake and wind loads can cause a greater acting force on the monopile of the OWT structure, which should be considered in the design phase and analysis.

It is noted that aerodynamic damping is not explicitly considered in this study. Although the calculated internal force (bending moment and shear force) can be slightly different from the situation considering all possible effects including the aerodynamic damping effect, it can be said that the coupled effect of wind and earthquake still needs attention.

5. Summaries and conclusions

To evaluate the dynamic performance of offshore wind turbines (OWTs) during the earthquake, the numerical model is built using the OpenSees framework with the PDMY03 soil constitutive model. The influences of soil-structure interaction (SSI), environmental load, and

soil liquefaction on the seismic response of the entire OWT system are investigated through a series of numerical simulations. The major findings obtained in this study are as follows.

1) The contribution of higher modes is becoming of increased importance in the seismic response of this 3 MW OWT. The amplification of acceleration is significant at the middle and transition piece locations of the OWT rather than at the tower head.
2) During the earthquake, soil liquefaction occurs in the shallow layer even for the dense sand, leading to the degradation of soil stiffness. A significant increase in the shear strain of soil elements in the liquefaction layer on the leeward side appears due to the existence of the deviatoric stress caused by the wind load.
3) Considering the soil-structure interaction (SSI) effect yields a larger dynamic response of the entire OWT system due to the kinematic interaction. Neglecting SSI will lead to the underestimation of the seismic response, which is harmful to the structure design.
4) The combined effect of the earthquake and lateral wind load can lead to severe deflection and tilt. The lateral displacement and rotation resulting from the combined action of wind and earthquake loads exceeds the sum of those observed under the individual actions of wind and earthquake.
5) Soil liquefaction makes a significant contribution to the development of lateral displacements and rotations under the combined wind and earthquake actions. Therefore, such a combined effect cannot be ignored in the design for the monopile-supported OWTs in the highly seismic regions.

The above findings emphasize that the coupled wind and earthquake loads have a considerable impact on the OWT. The occurrence of soil liquefaction during an earthquake leads to a reduction in the lateral capacity of the monopile, which is detrimental to the OWT subjected to the lateral wind load, as the values of the maximum horizontal displacement, rotation angle and bending moment are increased considerably. Consequently, it is essential to take the combined effect of the earthquake and wind loads into account in the design phase and analysis for OWTs will be built in the highly seismic regions However, it should be noted that the wave load is neglected in this study, which can lead to the discrepancy of the performance of the OWT. In reality, influenced by the wind speed, which accelerates the wave propagation rate and increases the wave height, the corresponding hydrodynamic pressure at the same water depth increases as the wind speed increases; therefore, the associated wave loads cannot be ignored [70]. Given the relatively high frequency of wave loads, treating them as constant loads is irrational. The application of time-variant wind loads and wave loads coupled with the seismic load in the transient analysis will be one of the future assignments. In addition, the capacity of the OWT nowadays has already reached 10 MW, and the corresponding size is also growing. The larger OWTs should be considered in the next step of the numerical analysis. Finally, in this study, only one seismic record (Tokachi-Oki earthquake) is considered. Different types of earthquake records with various amplitudes and frequencies should be considered in future research to enhance the generality of the conclusions.

CRediT authorship contribution statement

Wentao He: Writing – original draft, Visualization, Validation, Methodology, Investigation, Formal analysis. **Akihiro Takahashi:** Writing – review & editing, Supervision, Resources, Methodology, Conceptualization.

Declaration of competing interest

The authors declare that they have no known competing financial interests or personal relationships that could have appeared to influence the work reported in this paper.

Acknowledgments

The first author sincerely acknowledges the support provided by Dr. Jiro Takemura, former Associate Professor, Department of Civil and Environmental Engineering, Tokyo Institute of Technology, Japan, for sharing the results of his centrifuge tests.

Data availability

Data will be made available on request.

References

[1] Wang X, Zeng X, Li X, Li J. Liquefaction characteristics of offshore wind turbine with hybrid monopile foundation via centrifuge modelling. Renew Energy 2020; 145:2358–72.
[2] Sahu BK, Hiloidhari M, Baruah DC. Global trend in wind power with special focus on the top five wind power producing countries. Renew Sustain Energy Rev 2013; 19:348–59.
[3] GWEC (Global Wind Energy Council). Global wind energy outlook 2016. 2017.
[4] WWEA (World Wind Energy Association). World wind energy association 2016. 2016.
[5] Kaynia AM. Seismic considerations in design of offshore wind turbines. Soil Dynam Earthq Eng 2019;124:399–407.
[6] Bilgili M, Yasar A, Simsek E. Offshore wind power development in Europe and its comparison with onshore counterpart. Renew Sustain Energy Rev 2011;15(2): 905–15.
[7] Markard J, Petersen R. The offshore trend: structural changes in the wind power sector. Energy Pol 2009;37(9):3545–56.
[8] Bonou A, Laurent A, Olsen SI. Life cycle assessment of onshore and offshore wind energy-from theory to application. Appl Energy 2016;180:327–37.
[9] Kaldellis JK, Apostolou D, Kapsali M, Kondili E. Environmental and social footprint of offshore wind energy. Comparison with onshore counterpart. Renew Energy 2016;92:543–56.
[10] Li J, Yu XB. Onshore and offshore wind energy potential assessment near Lake Erie shoreline: a spatial and temporal analysis. Energy 2018;147:1092–107.
[11] Kamada Y, Maeda T, Murata J, Iida K, Okumura Y. Fundamental study on aerodynamic force of floating offshore wind turbine with cyclic pitch mechanism. Energy 2016;99:20–31.
[12] Wang H, Wang L, Hong Y, Mašín D, Li W, He B, Pan H. Centrifuge testing on monotonic and cyclic lateral behavior of large-diameter slender piles in sand. Ocean Eng 2021;226:108299.
[13] Cohen A. As global energy demands grows. So does appetite for offshore wind accessed. 2019. https://www.forbes.com/sites/arielcoh.en/2019/03/26/as-global-energy-demands-grows-so-does-appetite-for-offsh.ore-wind/#3247073265e7. [Accessed 1 March 2020].
[14] Zhang Y, Liu H, Wu W, Wang L, Jiang G. A 3D analytical model for distributed low strain test and parallel seismic test of pipe piles. Ocean Eng 2021;225:108828.
[15] Europe W. The European offshore wind industry: key trends and statistics 2016. Brussels, Belgium: Wind Europe; 2017. p. 37.
[16] Takahashi A, Omura N, Kobayashi T, Kamata Y, Inagaki S. Centrifuge model tests on large-diameter monopiles in dense sand subjected to two-way lateral cyclic loading in short-term. Soils Found 2022;62(3):101148.
[17] Wang H, Lehane BM, Bransby MF, Wang LZ, Hong Y. Field and numerical study of the lateral response of rigid piles in sand. Acta Geotechnica 2022;17(12):5573–84.
[18] Wang H, Fraser Bransby M, Lehane BM, Wang L, Hong Y. Numerical investigation of the monotonic drained lateral behaviour of large-diameter rigid piles in medium-dense uniform sand. Geotechnique 2021;73(8):689–700.
[19] Wang H, Lehane BM, Bransby MF, Wang LZ, Hong Y, Askarinejad A. Lateral behavior of monopiles in sand under monotonic loading: insights and a new simple design model. Ocean Eng 2023;277:114334.
[20] Arany L, Bhattacharya S, Macdonald J, Hogan SJ. Design of monopiles for offshore wind turbines in 10 steps. Soil Dynam Earthq Eng 2017;92:126–52.
[21] Katsanos EI, Thöns S, Georgakis CT. Wind turbines and seismic hazard: a state-of-the-art review. Wind Energy 2016;19(11):2113–33.
[22] Prowell I, Uang CM, Elgamal A, Luco JE, Guo L. Shake table testing of a utility-scale wind turbine. J Eng Mech 2012;138(7):900–9.
[23] Haenler M, Ritschel U, Warnke I. Systematic modelling of wind turbine dynamics and earthquake loads on wind turbines. In: European wind energy conference and exhibition. Athens, Greece: European Wind Energy Association; 2006, February. p. 1–6.
[24] Liu Y, Li X, Shi W, Wang W, Jiang Z. Vibration control of a monopile offshore wind turbines under recorded seismic waves. Renew Energy 2024;226:120455.
[25] Cheng X, Wang T, Zhang J, Wang P, Tu W, Li W. Dynamic response analysis of monopile offshore wind turbines to seismic and environmental loading considering the stiffness degradation of clay. Comput Geotech 2023;155:105210.
[26] Esfeh PK, Kaynia AM. Earthquake response of monopiles and caissons for Offshore Wind Turbines founded in liquefiable soil. Soil Dynam Earthq Eng 2020;136: 106213.
[27] Xi R, Xu C, Du X, El Naggar MH, Wang P, Liu L, Zhai E. Framework for dynamic response analysis of monopile supported offshore wind turbine excited by combined wind-wave-earthquake loading. Ocean Eng 2022;247:110743.

[28] Español-Espinel C, Haigh SK, Madabhushi GS, Abadie CN, Go JE, Morrison PR. Evolution of excess pore water pressures around monopiles subjected to moderate seismic loading. Soil Dynam Earthq Eng 2024;176:108316.
[29] Mazzoni S, McKenna F, Scott MH, Fenves GL. OpenSees command language manual. Pacific earthquake engineering research (PEER) center 2006;264(1):137–58.
[30] Takeuchi K, Takemura J. Examination of extended similarity rule on physical model of short pile subject to horizontal force. The 54th Japan National Conference on Geotechnical Engineering 2019 [in Japanese)].
[31] Takemura J, Kondoh M, Esaki T, Kouda M, Kusakabe O. Centrifuge model tests on double propped wall excavation in soft clay. Soils Found 1999;39(3):75–87.
[32] Elgamal A, Yan L, Yang Z, Conte JP. Three-dimensional seismic response of Humboldt Bay bridge-foundation-ground system. J Struct Eng 2008;134(7):1165–76.
[33] Zhang X, Tang L, Ling X, Chan AHC, Lu J. Using peak ground velocity to characterize the response of soil-pile system in liquefying ground. Eng Geol 2018;240:62–73.
[34] Takahashi A. Seismic performance evaluation of pile-supported wharf by 3D finite element analysis. In: Proceedings of the 12th Asian regional conference on soil mechanics and geotechnical engineering; 2003. p. 245–8. Singapore.
[35] Anastasopoulos I, Theofilou M. Hybrid foundation for offshore wind turbines: environmental and seismic loading. Soil Dynam Earthq Eng 2016;80:192–209.
[36] Yang Z, Elgamal A, Parra E. Computational model for cyclic mobility and associated shear deformation. J Geotech Geoenviron Eng 2003;129(12):1119–27.
[37] Khosravifar A, Elgamal A, Lu J, Li J. A 3D model for earthquake-induced liquefaction triggering and post-liquefaction response. Soil Dynam Earthq Eng 2018;110:43–52.
[38] Japanese Geotechnical Society. Japanese standards and explanations of laboratory tests of geomaterials 2 of 2. Part 2009;5:719–20 [in Japanese)].
[39] Biot MA. Theory of elasticity and consolidation for a porous anisotropic solid. J Appl Phys 1955;26(2):182–5.
[40] Law HK, Lam IP. Application of periodic boundary for large pile group. J Geotech Geoenviron Eng 2001;127(10):889–92.
[41] Kumar R, Sawaishi M, Horikoshi K, Takahashi A. Centrifuge modeling of hybrid foundation to mitigate liquefaction-induced effects on shallow foundation resting on liquefiable ground. Soils Found 2019;59(6):2083–98.
[42] Kumar R, Horikoshi K, Takahashi A. Centrifuge testing to investigate effects of partial saturation on the response of shallow foundation in liquefiable ground under strong sequential ground motions. Soil Dynam Earthq Eng 2019;125:105728.
[43] Fard MM, Erken A, Erkmen B, Ansal A. Analysis of offshore wind turbine by considering soil-pile-structure interaction: effects of foundation and sea-wave properties. J Earthq Eng 2022;26(14):7222–44.
[44] Fard MM, Erken A, Ansal A. Dynamic assessment of OWT under coupled seismic and sea-wave motions. Sustainable Marine Structures 2023;5(2):38–46.
[45] Colherinhas GB, de Morais MVG, Machado MR. Spectral model of offshore wind turbines and vibration control by pendulum tuned mass dampers. Int J Struct Stabil Dynam 2022;22(5):2250053.
[46] Zhang Z, De Risi R, Sextos A. Multi-hazard fragility assessment of monopile offshore wind turbines under earthquake, wind and wave loads. Earthq Eng Struct Dynam 2023;52(9):2658–81.
[47] Wang W, Gao Z, Li X, Moan T. Model test and numerical analysis of a multi-pile offshore wind turbine under seismic, wind, wave, and current loads. J Offshore Mech Arctic Eng 2017;139(3):031901.
[48] Ueda K, Uzuoka R, Iai S, Okamura T. Centrifuge model tests and effective stress analyses of offshore wind turbine systems with a suction bucket foundation subject to seismic load. Soils Found 2020;60(6):1546–69.
[49] Humire F, Ziotopoulou K. Mechanisms of shear strain accumulation in laboratory experiments on sands exhibiting cyclic mobility behavior. Can Geotech J 2022;59(8):1401–13.
[50] Shamoto Y, Zhang JM, Goto S. Mechanism of large post-liquefaction deformation in saturated sand. Soils Found 1997;37(2):71–80.
[51] Tomasello G, Porcino DD. Influence of sloping ground conditions on cyclic liquefaction behavior of sand under simple shear loading. Soil Dynam Earthq Eng 2022;163:107516.
[52] Umar M, Chiaro G, Kiyota T, Ullah N. Deformation and cyclic resistance of sand in large-strain undrained torsional shear tests with initial static shear stress. Soils Found 2021;61(3):765–81.
[53] Lu Z, Zhao S, Ma C, Dai K. Experimental and analytical study on the performance of wind turbine tower attached with particle tuned mass damper. Eng Struct 2023;294:116784.
[54] Turbines-Part W. 3: design requirements for offshore wind turbines. Proceedings of the IEC. 2009. p. 61400–3.
[55] Alkhoury P, Soubra AH, Rey V, Aït-Ahmed M. A full three-dimensional model for the estimation of the natural frequencies of an offshore wind turbine in sand. Wind Energy 2021;24(7):699–719.
[56] Kaynia AM. Effect of kinematic interaction on seismic response of offshore wind turbines on monopiles. Earthq Eng Struct Dynam 2021;50(3):777–90.
[57] Álamo GM, Aznárez JJ, Padrón LA, Martínez-Castro AE, Gallego R, Maeso O. Dynamic soil-structure interaction in offshore wind turbines on monopiles in layered seabed based on real data. Ocean Eng 2018;156:14–24.
[58] Demirci HE, Jalbi S, Bhattacharya S. Liquefaction effects on the fundamental frequency of monopile supported offshore wind turbines (OWTs). Bull Earthq Eng 2022;20(7):3359–84.
[59] Rodríguez-Galván E, Álamo GM, Medina C, Maeso O. Influence of seabed profile on the seismic response of monopile-supported offshore wind turbines including dynamic soil-structure interaction. Mar Struct 2023;92:103500.
[60] Sah UK, Yang J. Importance of higher modes for dynamic soil structure interaction of monopile-supported offshore wind turbines. Earthq Eng Struct Dynam 2024;53(6):2006–31.
[61] Ju SH. Studying the mode shape participation factor of wave loads for offshore wind turbine structures. Eng Struct 2024;310:118067.
[62] Corciulo S, Zanoli O, Pisanò F. Transient response of offshore wind turbines on monopiles in sand: role of cyclic hydro–mechanical soil behaviour. Comput Geotech 2017;83:221–38.
[63] Fard MM, Erken A, Erkmen B, Ansal A. Analysis of offshore wind turbine by considering soil-pile-structure interaction: effects of foundation and sea-wave properties. J Earthq Eng 2022;26(14):7222–44.
[64] De Risi R, Bhattacharya S, Goda K. Seismic performance assessment of monopile-supported offshore wind turbines using unscaled natural earthquake records. Soil Dynam Earthq Eng 2018;109:154–72.
[65] Reyno H, Park JS, Kang YJ. Influence of door opening and collar stiffener on the buckling capacity of cylindrical wind tower. Indian J Sci Technol 2015;8(25):1–7.
[66] Medina C, Álamo GM, Padrón LA. Contribution of the rotational kinematic interaction to the seismic response of monopile-supported offshore wind turbines. Ocean Eng 2023;280:114778.
[67] He K, Ye J. Seismic dynamics of offshore wind turbine-seabed foundation: insights from a numerical study. Renew Energy 2023;205:200–21.
[68] DNV D. OS-J101. Design of offshore wind turbine structures. Revision Proposal; 2007.
[69] DNV D. RP-0585 seismic design of wind power plants. 2021.
[70] Wang P, Yu W, Zhao M, Du X. Effects of wind-wave-current-earthquake interaction on the wave height and hydrodynamic pressure based on CFD method. Ocean Eng 2024;305:117909.